



Deposited via The University of Leeds.

White Rose Research Online URL for this paper:

<https://eprints.whiterose.ac.uk/id/eprint/182335/>

Version: Accepted Version

Article:

Song, B, Hua, Y, Zhou, C et al. (2022) Fabrication and anticorrosion behavior of a bi-phase TaNbHfZr/CoCrNi multilayer coating through magnetron sputtering. *Corrosion Science*, 196. 110020. ISSN: 0010-938X

<https://doi.org/10.1016/j.corsci.2021.110020>

© 2021 Elsevier Ltd. All rights reserved. This manuscript version is made available under the CC-BY-NC-ND 4.0 license <http://creativecommons.org/licenses/by-nc-nd/4.0/>.

Reuse

This article is distributed under the terms of the Creative Commons Attribution-NonCommercial-NoDerivs (CC BY-NC-ND) licence. This licence only allows you to download this work and share it with others as long as you credit the authors, but you can't change the article in any way or use it commercially. More information and the full terms of the licence here: <https://creativecommons.org/licenses/>

Takedown

If you consider content in White Rose Research Online to be in breach of UK law, please notify us by emailing eprints@whiterose.ac.uk including the URL of the record and the reason for the withdrawal request.

1 **Fabrication and anticorrosion behavior of a bi-phase**
2 **TaNbHfZr/CoCrNi multilayer coating through magnetron sputtering**

3 Baorui Song^{1,3}, Yong Hua^{*2}, Chaozheng Zhou¹, Yanhuai Li¹, Liuquan Yang³,
4 Zhongxiao Song^{*1}

5 1: State Key Laboratory for Mechanical Behavior of Materials, Xi'an Jiaotong
6 University, Xi'an 710049, Shaanxi, P.R. China.

7 Email: zhongxiaosong@mail.xjtu.edu.cn

8 2: Corrosion and Integrity Centre, Zhejiang JIULI Hi-Tech Metals Co. Ltd, Hu Zhou,
9 P.R. China.

10 Email: leo.huayong@gmail.com

11 3: Institute of Functional Surfaces, School of Mechanical Engineering, University of
12 Leeds, Leeds LS2 9JT, United Kingdom

13 *: Authors to whom correspondence should be addressed.

14 **Keywords:** high entropy alloy, multilayer coating, magnetron sputtering, corrosion
15 properties

16 **Abstract**

17 A novel multilayer coating containing bi-phase structures was designed via a
18 magnetron sputtering method. Surface morphologies, phase structure and corrosion
19 behavior of TaNbHfZr/CoCrNi coating have been investigated via a combination of
20 electrochemistry and surface analysis. Such bi-phase structures containing fcc
21 CoCrNi and amorphous TaNbHfZr layers exhibited an improved corrosion resistance
22 compared with CoCrNi monolayer coating. The hardness and elastic modulus of the
23 TaNbHfZr/CoCrNi multilayer coating were slightly lower than the CoCrNi monolayer
24 coating due to the softening induced by the amorphous TaNbHfZr layer, revealing that
25 such multilayer structure possesses the desired corrosion performance and maintains
26 good mechanical properties.

27 **Keywords:** Coating; Corrosion; HEAs; MEAs; magnetron sputtering

28 **1. Introduction**

29 The high entropy alloys (HEAs) with simple microstructure but complex stoichiometry
30 were firstly defined by Yeh et al. in 2004 [1]. The definition of HEAs composes of five
31 or more metal elements such as Cr, Co, Fe, Mo, etc., with the concentration of each
32 element in the range of 5~35 at.% [1]. In recent years, researchers have reported on
33 the exploration of various HEAs or medium entropy alloys (MEAs) with superior
34 properties such as excellent corrosion resistance [2, 3], high strength or hardness [4]
35 and high stability [5]. It is imperative to open the pathway for a broader practical
36 application, especially in the structural field and long-term engineering applications
37 requiring an outstanding combination of both mechanical and corrosion performance.
38 The “cocktail effect” was considered for HEAs/MEAs to integrate functional elements
39 into a different and specific utilization [6, 7]. The incorporation of passivating elements
40 Cr, Ni, Co, Mo, etc. can enhance the corrosion resistance, the addition of refractory
41 Ta, Nb, Cr, etc. can improve the mechanical performance or the stability in extreme
42 environments [8]. As reported in our previous work, the hardness of the TaNbHfZr
43 amorphous coating reaches ~8 GPa [9]. Shi et al. [10] have reported that CoCrNi MEA
44 with face-centered cubic (fcc) structure has excellent strength and toughness as well
45 as corrosion resistance, which are considered as the basic components for the
46 promising engineering alloys demanding in the extreme and highly-sensitive
47 engineering service environments. Wang et al. [11] compared bulk CoCrNi MEA with
48 304 (SS), the results found that CoCrNi exhibited superior corrosion resistance in a 1
49 M H₂SO₄ solution and Co oxides were found as the main constituents within the
50 passive film.

51 The conventional approaches to fabricate HEAs/MEAs are mainly by arc melting or
52 casting with high cost due to the complicated fabrication processes [12]. It has been
53 reported that the HEA/MEA coatings which are compositionally the same as the bulk
54 material manufactured via conventional approach, while possessing better corrosion-
55 resistant properties [13], also nearly twice the hardness compared to that of bulk
56 materials [14, 15]. Feng et al. [12] reported that the laser clad CoCrNi coating
57 possessed a more positive passive potential in a 0.5 M H₂SO₄ solution.

58 Recently, a growing number of investigations have been focused on HEA/MEA
59 coatings. Magnetron sputtering (MS), as one of the physical vapor deposition (PVD)
60 methods, has been widely used to fabricate coatings in aerospace [16-18], automotive
61 [19], cutting tools [20] and watches [21], etc. Comparatively, MS possesses the “rapid
62 quenching effect” with a fast cooling rate which can restrict the diffusion of elements
63 and thus restrain the nucleation and growth of intermetallic compounds, in favor of the
64 formation of HEA/MEA solid-solution [22, 23], therefore, more homogeneous, dense
65 microstructure and uniform compositional distribution can be obtained in the HEA/MEA
66 coatings via MS methods [24] and also the use of MS to fabricate HEA/MEA coating
67 is more environmentally friendly than traditional melting or casting approaches [25].
68 However, in the monolayer coating, the columnar structure and defects such as voids,
69 pinholes, pores or cracks can lead to open paths between the substrate and the
70 corrosive environment [26, 27].

71 Structural design of HEA/MEA coatings can be optimized for stability and corrosion
72 resistance, the mixing entropy contributes to the formation of solid solutions with
73 fcc, body-centered cubic (bcc), hexagonal closest packed (hcp), or amorphous
74 structure. The high mixing entropy enhances the mutual solubility of various elements
75 and prevents phase segregation, meanwhile, the large atomic size difference causes
76 severe lattice distortion and favors the amorphous structure due to the local elastic
77 strain [28]. It has been reported that the amorphous structure is beneficial to the
78 corrosion resistance of the functional coatings due to the absence of grain boundary
79 than the corresponding crystalline structure [22]. Therefore, a simple and robust
80 strategy to combine HEA/MEA with amorphous structures in a multilayer coating with
81 harder and better corrosion resistance is still necessary to enable its practical
82 application. The multilayer structure can effectively reduce stress concentration [29],
83 and large number of interfaces can block the growth of coarse columnar grain making
84 the coating more compact [30], preventing the propagation of cracks or pores and
85 improving the overall performance.

86 Herein, an innovative strategy via PVD methodology was implemented to fabricate a
87 functionally anticorrosive multilayer coating. The corrosion resistance was

88 substantially improved by a multilayer coating combining CoCrNi MEA with TaNbHfZr
89 high entropy metallic glass layers, which also retains the mechanical performance at
90 a good level. The corrosion behavior and mechanical properties of the developed
91 coatings were investigated by a series of surface analysis, nanoindentation and
92 electrochemical tests.

93 **2. Experimental**

94 **2.1 Material manufacture via PVD methods**

95 The multilayer TaNbHfZr/CoCrNi coating was prepared by DC magnetron sputtering
96 using equiatomic CoCrNi ternary and quaternary TaNbHfZr targets (Φ 75 mm \times 5 mm),
97 which were made via powder metallurgy with purities >99.99 %. For comparison, a
98 monolayer CoCrNi or TaNbHfZr coating with the same thickness was also prepared.
99 P-type (100) Si wafers and 304 SS were chosen as substrates for microstructural
100 characterization and electrochemical tests, respectively. The base pressure prior to
101 the deposition was less than 5×10^{-4} Pa. Prior to deposition, the surface of 304 SS was
102 ground up to 3000 # SiC papers, followed by mirror finishing via the diamond polishing
103 spray on a flannel cloth to reduce the surface roughness ($R_a \sim 3$ nm), and then cleaned
104 ultrasonically using acetone and alcohol for 15 mins. During deposition, Ar flow rate
105 was kept at 30 sccm and the working pressure was 0.45 Pa; the bias was set as -70
106 V, which is optimized to ensure good adhesion between the coatings and the
107 substrates; the DC powers were 150 W and 120 W for TaNbHfZr layer and CoCrNi
108 layer, respectively. Each CoCrNi or TaNbHfZr layer was deposited in sequence to form
109 the multilayer TaNbHfZr/CoCrNi coating and the whole deposition process of the
110 multilayer was continuous layer by layer in a vacuum environment thus the multilayer
111 was an integrated coating, and the thickness of each layer was controlled by the
112 deposition time.

113 **2.2 Surface analysis**

114 The phase structure was characterized by an x-ray diffractometer (XRD) with Cu $K\alpha$
115 radiation on a Bruker D8 Discover powder x-ray diffractometer. High-resolution
116 transmission electron microscopy (HRTEM, JEM-2100F) experiments were performed

117 to investigate the cross-sectional microstructure. Scanning electron microscopy (SEM,
118 FEI-VERIOS460) with EDS (Energy Dispersive Spectrometer) was employed to
119 observe the top surface, cross-sectional morphologies and the elemental distribution,
120 respectively. The surface morphology of pitting was observed by Nikon MA200 Optical
121 Microscope. Chemical compositions of the passive layer on the surface are analyzed
122 by XPS (Thermo Fisher ESCALAB Xi+) with a monochromatic Al $K\alpha$ X-ray source of
123 2 KeV at a take-off angle of 54.7°. The beam spot size was 500 μm . The pass energy
124 was 20.0 eV with an energy step size of 0.1 eV. The measured binding energies were
125 calibrated regarding the C 1s peak with a binding energy value of 284.8 eV.

126 **2.3 Mechanical properties**

127 Nanoindentation was carried out on a Ti950 TriboIndenter (Hysitron, Minneapolis, MN)
128 using a calibrated diamond Berkovich indenter. Load control mode was set with the
129 peak force of 5 mN with loading time of 5 s, holding time of 2 s, and unloading time of
130 5 s, respectively. 9 points were measured for each sample to obtain the average value
131 of the results in order to ensure repeatability and reliability. The hardness H and
132 reduced elastic modulus E_r were analyzed using the Oliver-Pharr method [31].

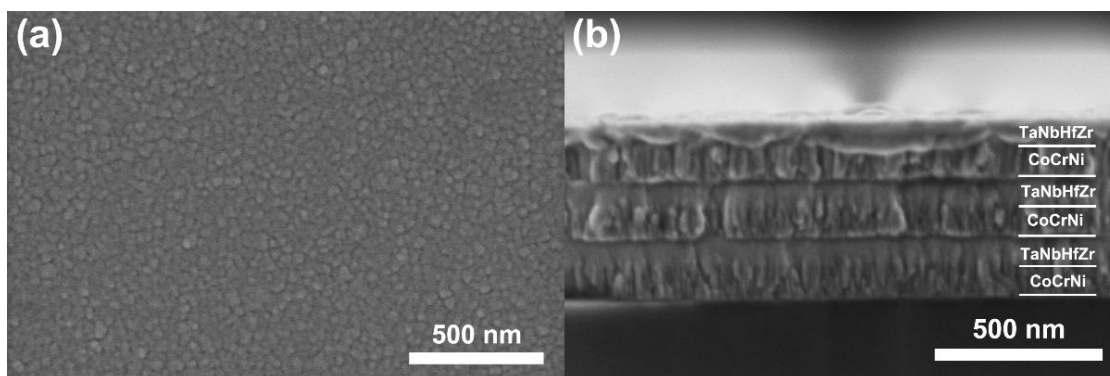
133 **2.4 Electrochemical measurements**

134 The electrochemical tests were performed in a 3.5 wt.% NaCl solution. A standard
135 three-electrode electrochemical cell with a platinum foil as a counter electrode,
136 Ag/AgCl as reference electrode, and the HEAs coated samples were used as working
137 electrodes. All electrochemical tests were performed using the Metrohm Autolab
138 workstation. Open-circuit potential (OCP) was recorded for 30 mins to reach a steady
139 state. The electrochemical impedance spectroscopy (EIS) measurements were
140 conducted at the OCP condition in a frequency range from 10^5 Hz down to 10^{-2} Hz
141 with the amplitude of 10 mV, the impedance data were analyzed using Zsimpwin
142 software. The potentiodynamic polarization measurements were carried out from -0.5
143 V_{OCP} to $1.0 V_{\text{OCP}}$ at a scan rate of 1 mV/s.

144 **3. Results and discussion**

145 **3.1 Surface characterization**

146 The top surface and cross-sectional morphologies of the multilayer TaNbHfZr/CoCrNi
147 coating are shown in **Figure 1**. Nano-size round sheet-like granules for
148 TaNbHfZr/CoCrNi coating were observed on the surface. For the composed CoCrNi
149 monolayer, the columnar grains were confirmed from the cross-sectional SEM images
150 as shown in **Figure 1 (b)**. It can be noted that the thickness of each monolayer was
151 100 nm, and the entire coating was 600 nm in thickness. The interfaces are explicitly
152 presented (**Figure 1b**), to indicate the existence of the well-constructed multilayer
153 structure. As shown in **Figure S1**, the strength of the TaNbHfZr/CoCrNi multilayer
154 coating was ~27.5 N with no obvious peeling-off of the coating observed during the
155 dynamic loading process, indicating a good adhesion strength between the coating
156 and substrate. The columnar grains were separated by the amorphous TaNbHfZr layer,
157 which can also be confirmed by the following TEM observation.

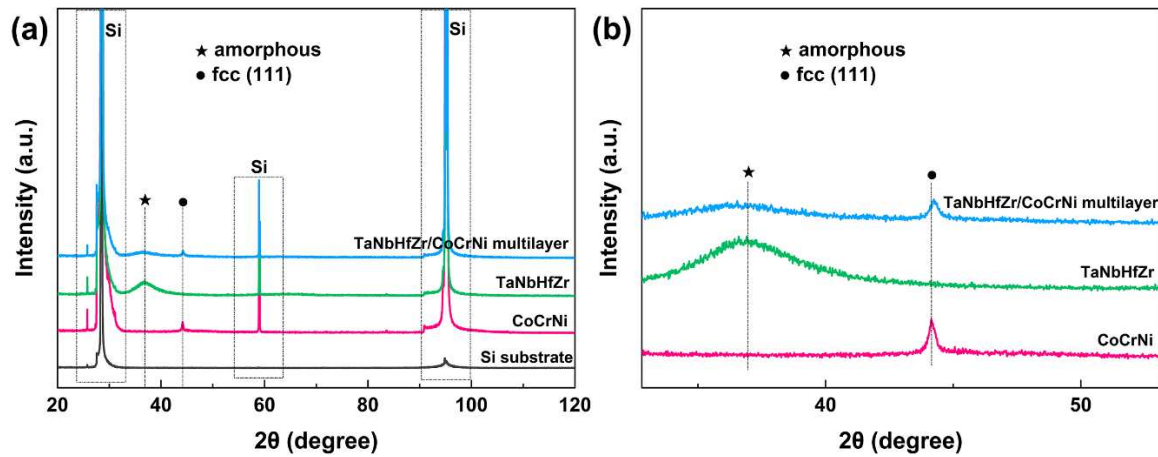


158 **Figure 1 (a)** Surface morphologies and **(b)** cross-sectional morphologies for
159 TaNbHfZr/CoCrNi multilayer coating.
160

161 **3.2 XRD measurements**

162 The overall XRD patterns of CoCrNi, TaNbHfZr monolayer and TaNbHfZr/CoCrNi
163 multilayer coatings are presented in **Figure 2**. After deducting the diffraction peaks for
164 Si (111) substrate, the CoCrNi monolayer demonstrates a single fcc structure with (111)
165 diffraction peak of preferred orientations at 44.1°. For TaNbHfZr monolayer, the broad
166 steamed bun-like peak at 37.0° was detected, which confirms the amorphous feature.
167 For TaNbHfZr/CoCrNi multilayer coating, two sets of diffraction peaks including the

168 crystalline CoCrNi and TaNbHfZr amorphous phase exist simultaneously. The
 169 diffraction peaks for fcc CoCrNi solid-solution is broad, suggesting that the grain size
 170 is small according to the Debye-Scherrer equation ($D = \frac{K\gamma}{B \cos \theta}$, where K is the Scherrer
 171 constant, D is the average grain size, γ is the wavelength of X-ray, θ is the Bragg angle),
 172 the results have good agreement with the SEM observation of the grain sizes as shown
 173 in **Figure 1 (a)**.

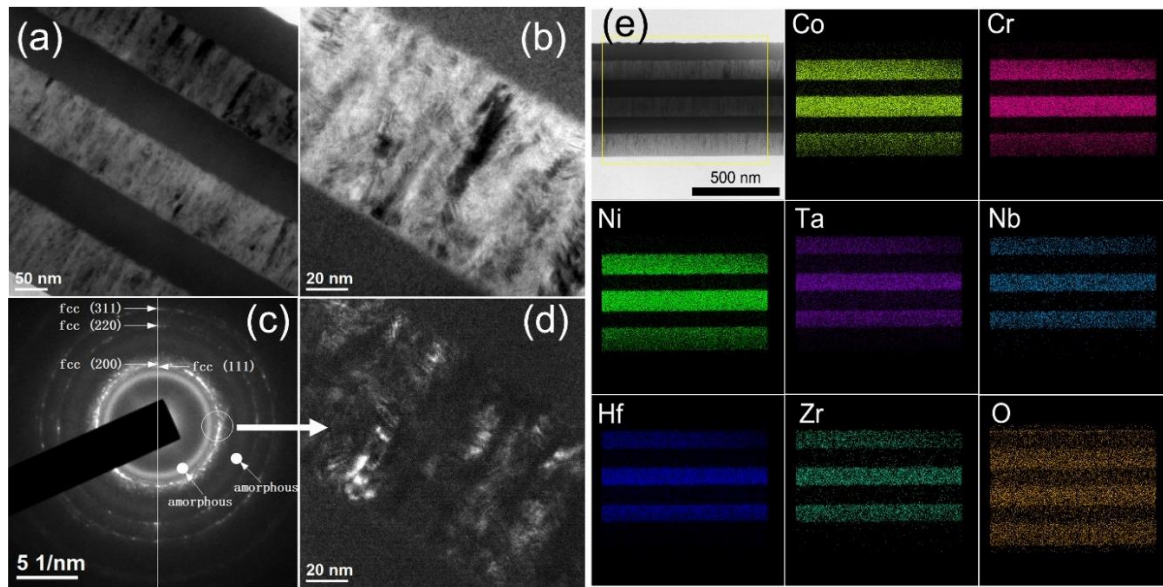


174
 175 **Figure 2 (a)** XRD patterns; **(b)** enlarged XRD patterns of as-deposited CoCrNi and
 176 TaNbHfZr/CoCrNi coatings.

177 **3.3 TEM analysis**

178 The TEM characterization of the multilayer TaNbHfZr/CoCrNi coating is illustrated in
 179 **Figure 3**. Clear interfaces and well adhesion between each layer were observed in
 180 **Figures 3 (a)** and **(b)**, suggesting the good compatibility between each deposited layer.
 181 SAED (Selected Area Electron Diffraction) image in **Figure 3 (c)** reveals that a
 182 combination of nano-polycrystalline (111), (200), (220), (311) of CoCrNi monolayer and
 183 no lattice phase contrast of amorphous TaNbHfZr monolayer were observed, which is
 184 consistent with the XRD patterns as shown in Figure 2. In the bright field (BF) image
 185 in **Figure 3 (b)** and DF (Dark Field) image shown in **Figure 3 (d)**, the grain size of 20
 186 nm in width and grain boundaries were identified. The EDS mapping result in **Figure**
 187 **3 (e)** implies that the multilayer coating has homogeneous elemental distribution
 188 without segregation and each TaNbHfZr or CoCrNi layer has the same chemical
 189 composition as shown in **Table 1**. The flat interfaces indicate good adhesion and

190 compatibility between each deposited layer.



191
 192 **Figure 3** (a) Low and (b) high magnification morphologies of layer structure; (c) SAED
 193 (selected area electron diffraction) image; (d) DF (dark field) image corresponding to
 194 the selected diffraction spots circled in (c), indicated by white arrow; (e) elemental
 195 distribution by EDS mapping for TaNbHfZr/CoCrNi multilayer coating.

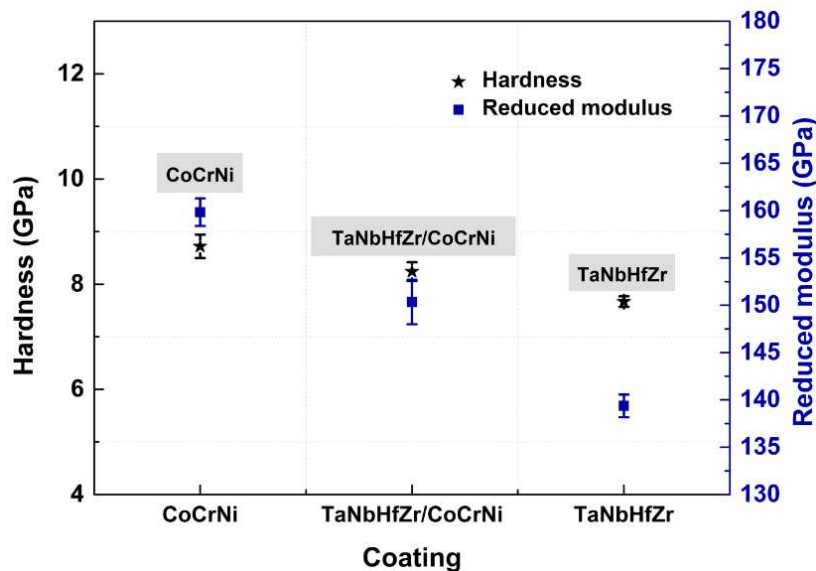
196 **Table 1** Elemental composition of TaNbHfZr and CoCrNi layer of the multilayer.

TaNbHfZr				CoCrNi		
Ta (at. %)	Nb (at. %)	Hf (at. %)	Zr (at. %)	Co (at. %)	Cr (at. %)	Ni (at. %)
27.27	29.62	22.81	20.30	29.59	36.42	33.98

197 **3.4 Mechanical property**

198 The nanoindentation tests at the peak load of 5 mN were carried out with the loading
 199 rate of 1 mN/s to compare the discrepancy of the mechanical behavior of CoCrNi and
 200 TaNbHfZr/CoCrNi coatings. The hardness and E_r are provided in **Figure 4**. The
 201 hardness is 7.67 GPa, 8.72 GPa and 8.24 GPa of TaNbHfZr, CoCrNi and
 202 TaNbHfZr/CoCrNi, respectively. In the amorphous TaNbHfZr, the shear bands cause
 203 the strain-softening due to the accumulation of the free volume by the inhomogeneous
 204 deformation [32]. For the multilayer coating, the introduction of the amorphous
 205 TaNbHfZr reduces the hardness, while the value is still higher than that in terms of the
 206 role-of-mixture indicating the interfaces play a role in the strengthening [33]. In the

207 nanoscale columnar grains, the dislocation needs to propagate within CoCrNi, thus
 208 the plastic yielding is determined by the required stress for single dislocation bowing
 209 via the confined layer slip (CLS) mechanism [32]. Besides, the interface may also have
 210 one or more arrays of misfit dislocations that will act as obstacles to CLS [34].
 211 Microscopy results confirm that the CoCrNi monolayer is 100 nm in thickness, while
 212 the grain size is 20 nm which is less than the total layer thickness, suggesting that the
 213 strengthening came more from grain boundaries rather than phase interfaces. The
 214 interfaces cut off the continuously-grown coarse columnar grains refining the grain size
 215 of each CoCrNi layer according to the film growth theory thus the Hall-Petch
 216 strengthening dominates [35]. The deformation mechanism transits from grain
 217 boundary strengthening, dislocation strengthening and solid solution strengthening in
 218 nanocrystalline structure to shear transformation with lack of the internal interfaces
 219 and a poorer strain hardening capability in an amorphous structure [36, 37], therefore,
 220 the hardness was reduced slightly of the TaNbHfZr/CoCrNi multilayer than the CoCrNi
 221 monolayer coating. The phase interfaces with disordered structure bring the inelastic
 222 strain in dual-phase multilayer can be responsible for the reduced E_r [36, 38].



223
 224 **Figure 4** Nanoindentation hardness and E_r for CoCrNi, TaNbHfZr monolayer and
 225 TaNbHfZr/CoCrNi multilayer coatings.

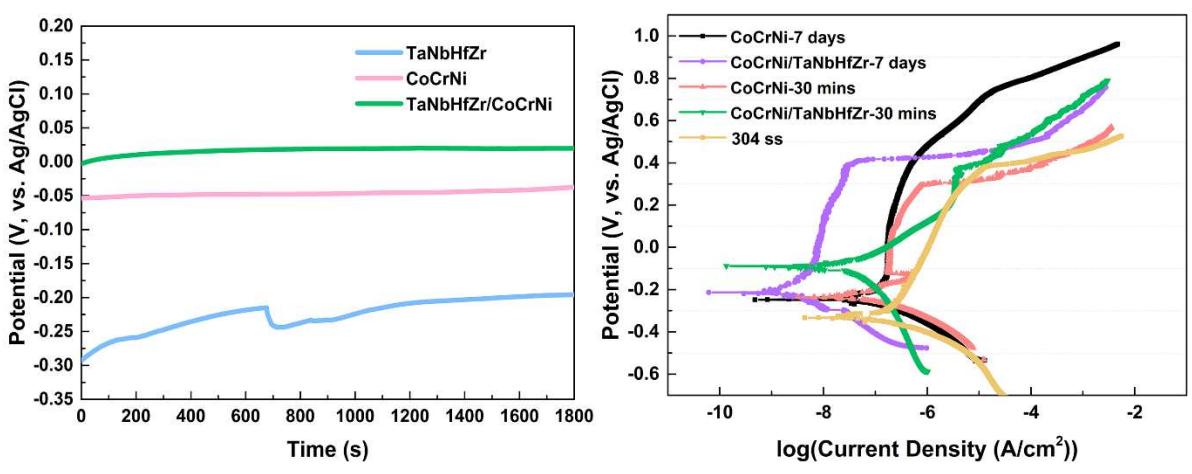
226 **3.5 Electrochemical performance**

227 **3.5.1 Potentiodynamic behavior of the samples immersed in a 3.5 wt. % NaCl** 228 **solution**

229 **Figure 5 (a)** displays OCP measurements of all the coatings for 1800 s and the typical
230 potentiodynamic polarization curves of CoCrNi and TaNbHfZr/CoCrNi coatings
231 immersed in the 3.5 wt.% NaCl solution at 25°C. It is clearly seen that the multilayer
232 coating exhibits more noble OCP in the stable state suggesting less tendency to be
233 corroded. Potentiodynamic polarization tests were employed to measure the
234 susceptibility of the material to the pitting resistance [39]. A summary of corrosion
235 potential (E_{corr}), current densities (i_{corr}) and pitting potential (E_{pit}) is provided in **Table**
236 **2**. The E_{corr} value of TaNbHfZr/CoCrNi multilayer coating is more positive compared to
237 that of the monolayer CoCrNi coating. The i_{corr} value of TaNbHfZr/CoCrNi coating at
238 the magnitude of 10^{-9} A/cm² is 2 orders lower than that of CoCrNi coating, suggesting
239 that the TaNbHfZr/CoCrNi coating is less prone to be corroded under the current
240 corrosive environment. A similar observation has been reported by Allahyarzadeh et
241 al. [39] that the corrosive species can be delayed during the diffusion process due to
242 the advantages of the multilayer structure. Therefore, compared with monolayer
243 CoCrNi, the multilayered TaNbHfZr/CoCrNi coating remains a better protective
244 capability to the substrate over a longer-time immersion in the solution.

245 Furthermore, the E_{pit} is denoted as the “knee” of the potential in the forward scan,
246 where corresponds to a rapid increase in current with a small change in potential.
247 When potential exceeds this value, pitting initiates, the more positive of E_{pit} , the more
248 pitting resistant for the material. After 7 days immersion, the E_{pit} of 0.40 V was recorded
249 for TaNbHfZr/CoCrNi coating, however, E_{pit} is not distinguished clearly for CoCrNi
250 coating. Here, the E_{pit} value of CoCrNi coating is taken as the current density reaches
251 $10 \mu\text{A}/\text{cm}^2$ [40]. The E_{pit} of CoCrNi (0.68 V) is more noble than that of TaNbHfZr/CoCrNi
252 (0.40 V), demonstrating a good resistance to pitting for CoCrNi monolayer coating.
253 Further investigation should be carried out on the modification of the microstructure
254 such as the modulation period or the modulation ratio to enhance the pitting resistance
255 of the multilayer coating. For instance, the interfaces of the multilayer coating with a

256 smaller modulation period can more effectively block the penetration of corrosive
 257 species (water molecules, Cl⁻).



258
 259 **Figure 5 (a)** OCP measurements for 30 mins, **(b)** typical potentiodynamic polarization
 260 plots for CoCrNi monolayer and TaNbHfZr/CoCrNi multilayer coatings after different
 261 immersion time in 3.5 wt.% NaCl solution.

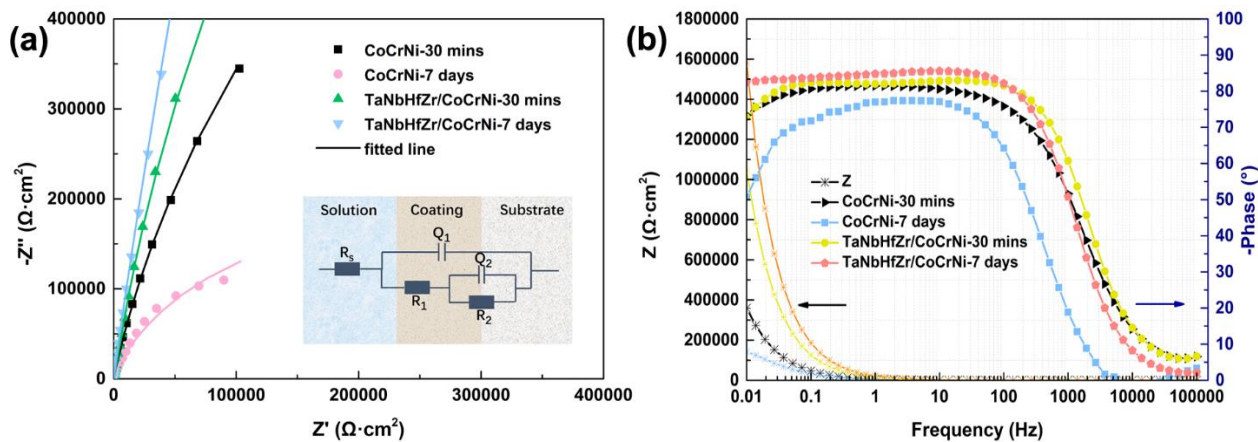
262 **Table 2** Electrochemical parameters obtained by potentiodynamic polarization tests
 263 for coatings immersed in the 3.5 wt.% NaCl solution at 25 °C after different immersion
 264 times.

Coating	Immersion time	E_{corr} (V, vs. Ag/AgCl)	i_{corr} ($\mu A/cm^2$)	E_{pit} (V vs. Ag/AgCl)
CoCrNi	30 mins	-0.24±0.002	$(5.79\pm 0.942)\times 10^{-1}$	0.30±0.010
	7 days	-0.25±0.002	$(6.79\pm 0.98)\times 10^{-1}$	0.68±0.040
TaNbHfZr/CoCrNi	30 mins	-0.09±0.003	$(7.8\pm 0.65)\times 10^{-3}$	0.34±0.014
	7 days	-0.21±0.006	$(4.78\pm 0.002)\times 10^{-3}$	0.40±0.010

265 **3.5.2 Electrochemical Impedance Spectroscopy (EIS)**

266 EIS was carried out to explore the corrosion properties and electrochemical processes
 267 of CoCrNi monolayer and CoCrNi/TaNbHfZr multilayer coatings as shown in **Figure6**.
 268 As demonstrated in **Figure 6 (a)**, the shape of these coatings are capacitive
 269 semicircles and the TaNbHfZr/CoCrNi coating has the largest semicircle after 7 days
 270 of exposure compared to that of 30 mins, indicating the increase in the corrosion
 271 resistance after long immersion. The Bode phase diagram implicates two time
 272 constants representing the rate of the electrochemical reactions [39] thus we utilized
 273 two RC components in the equivalent electrical circuit (EEC). The EEC model adopted

274 for fitting the EIS data is $R_s(Q_1(R_1(Q_2R_2)))$ as shown in **Figure 6 (a)** and the fitting
 275 quality is good with small chi-square values. The detailed fitted parameters are
 276 displayed in **Table 3**.



277
 278 **Figure 6 (a)** Experimental and fitted Nyquist plots; **(b)** Bode plots for CoCrNi
 279 monolayer and TaNbHfZr/CoCrNi multilayer coatings.

280 R_s represents the solution resistance. The constant phase element CPE in the
 281 equivalent circuit, designated as Q_1 and Q_2 , describing the frequency dispersion and
 282 deviation from the ideal dielectric behavior caused by the surface heterogeneity of the
 283 electrode, is expressed as [41, 42]

$$Z_{CPE} = \frac{1}{Y_0(j\omega)^n} \quad \text{Equation 1}$$

285 Where, $Y_0(Q)$ is the magnitude of CPE , ω is the angular frequency and n is the
 286 deviation parameter which lies in a value region between 0 and 1. when $n = 1$, the
 287 CPE is considered as an ideal capacitor; when $0.5 < n < 1$, the CPE describes a
 288 distribution of dielectric relaxation times in frequency space; When $n = 0.5$, the CPE
 289 represents a Warburg impedance. Here, the parameter of CPE represents the surface
 290 heterogeneity indicating the compactness of the coating and a lower Y_0 reveals the
 291 formation of a more homogeneous and less defective oxide film on the surface. The
 292 smaller R_2 and bigger $Y_0(Q_2)$ suggest the corrosion processes at the inner interfaces
 293 were more heterogeneous [43].

294 **Table 3** Fitted results of the EIS data.

Coating	R_s	Q_1	R_1	Q_2	$R_2 (\Omega \cdot \text{cm}^2)$	Chsq
---------	-------	-------	-------	-------	----------------------------------	------

(immersion time)	($\Omega \cdot \text{cm}^2$)	Y_0 ($\mu\text{F} \cdot \text{s}^{n-1} \cdot \text{cm}^{-2}$)	n	($\Omega \cdot \text{cm}^2$)	Y_0 ($\mu\text{F} \cdot \text{s}^{n-1} \cdot \text{cm}^{-2}$)	n		
CoCrNi (30 mins)	6.55±0.03	19.54±0.56	0.91± 0.002	8.38±0.02	12.60± 0.09	0.90± 0.01	(2.76± 0.06)×10 ⁶	4.3×10 ⁻⁴
CoCrNi (7 days)	26.64±1.49	18.44±0.12	0.98± 0.020	(3.37± 0.05)×10 ²	29.30± 0.08	0.73± 0.02	(4.73± 0.04)×10 ⁵	3.5×10 ⁻³
TaNbHfZr/CoCrNi (30 mins)	11.53±0.16	11.05±0.03	0.94± 0.003	(1.03± 0.02)×10 ⁵	1.24± 0.02	0.90± 0.02	(5.32± 0.05)×10 ⁶	5.3×10 ⁻⁴
TaNbHfZr/CoCrNi (7 days)	21.39±0.35	7.57±0.06	0.96± 0.003	(1.59± 0.03)×10 ⁵	0.88± 0.02	0.72± 0.01	(4.99± 0.02)×10 ⁸	3.7×10 ⁻⁵

295 The whole polarization resistance for the system R_p , an index representing the
296 corrosion resistance of the coating system, was calculated via the following formula
297 [44]

$$R_p = R_1 + R_2 \quad \text{Equation 2}$$

298
299 R_1 and Q_1 represent the electric double layer resistance and capacitance between the
300 HEA coatings and the solution at the high frequency, R_2 and Q_2 are the charge transfer
301 resistance and the double-layer capacitance of the inner interfaces between the film
302 and the substrate at the low frequency. The lower R_p of TaNbHfZr/CoCrNi coating
303 signifies that the reduced corrosion resistance, the opposite trend of CoCrNi coating
304 interpreting the fact that TaNbHfZr/CoCrNi coating benefits from the multilayer
305 structure.

306 In the Bode plots as shown in **Figure 6 (b)**, the impedance modulus remains a straight
307 line and the phase angle is close to zero at high-frequency ranges, indicating the
308 resistive-like behavior. At the relatively low frequencies, a slanted impedance modulus
309 and a maximum phase angle are reached, indicating the capacitive-like behavior [45].
310 The higher the maximum phase angle, the better the corrosion properties. The
311 multilayer coating of TaNbHfZr/CoCrNi after 7 days' immersion possesses the superior
312 corrosion resistance with $|Z|$ of $1.5 \times 10^6 \Omega \cdot \text{cm}^2$ and the largest maximum phase angle
313 (85°) at low and medium frequencies from 0.01 Hz to ~100 Hz. The $|Z|$ values at the
314 frequency of 0.1 Hz corresponds to the polarization resistance which reflects the
315 corrosion resistance of the alloy in the solution [2]. The $|Z|$ value of TaNbHfZr/CoCrNi
316 at 0.1 Hz is higher than that of CoCrNi coating after different immersion times as

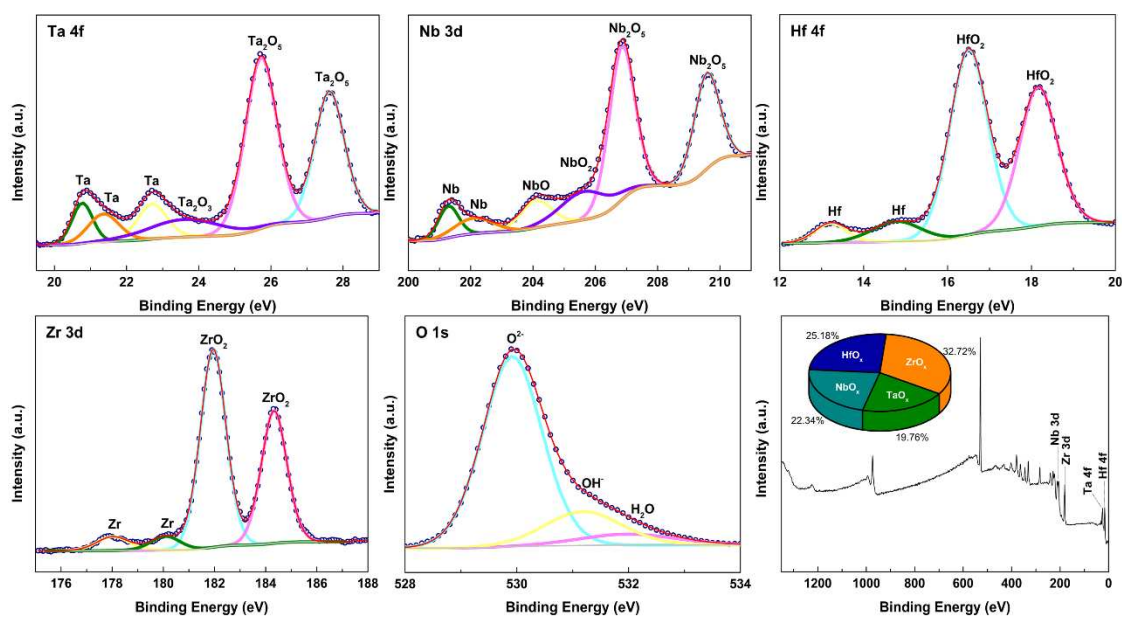
317 exhibited in **Figure 6 (b)**, suggesting that the corrosion resistance of TaNbHfZr/CoCrNi
318 multilayer coating is better.

319 **3.6 Characterization of the passive films**

320 **3.6.1 XPS result of the passive films**

321 To further examine the oxidation state of the passive film formed on the surface after
322 7 days' immersion, XPS analysis was conducted. The high-resolution spectrum of Ta
323 4f, Nb 3d, Hf 4f, Zr 3d and O 1s at the top surface are presented in **Figure 7**. To
324 improve the accuracy of the result, all the data has been calibrated by the stand
325 binding energy of C 1s peak of 284.8 eV. The Ta 4f spectrum split into the peaks at
326 27.62 eV and 25.73 eV corresponds to Ta 4f_{5/2} and Ta 4f_{7/2} of Ta₂O₅, simultaneously
327 minor Ta₂O₃ (23.60 eV) exists. The Nb 3d_{3/2} (209.57 eV) and Nb 3d_{5/2} (206.85 eV) of
328 the full oxide Nb₂O₅ accompanied by minor suboxide NbO₂ (205.63 eV) and NbO
329 (204.10 eV), the Hf 4f_{5/2} (18.16 eV) and Hf 4f_{7/2} (16.50 eV) for the full oxide HfO₂, the
330 Zr 3d_{3/2} (184.33 eV) and Zr 3d_{5/2} (181.95 eV) for full oxide ZrO₂ were also detected on
331 the surface. The results confirmed the stable chemical state of the oxide formed on
332 the surface, which is a vital contribution to the passive performance of
333 TaNbHfZr/CoCrNi coating. Apart from the oxides, the metallic states of Ta, Nb, Hf and
334 Zr were also detected. The percentage of the compositional oxides within the passive
335 films for TaNbHfZr/CoCrNi coating exhibits that the accounts of ZrO_x (32.72 at. %) are
336 higher than those of TaO_x (19.76 at. %), NbO_x (22.34 at. %) and HfO_x (25.18 at. %).
337 Moreover, the O 1s spectra are split into three peaks including O²⁻ (529.92 eV) species,
338 OH⁻ (531.19 eV) species and a small percentage of H₂O (531.98 eV) species,
339 suggesting the main presence of oxide and hydroxide on the surface of the coatings
340 with minor bound water to capture the dissolving metal ions forming a new film
341 resisting further corrosive attack [46]. For 7-day immersed CoCrNi monolayer coating,
342 as can be seen in **Figure S2**, the Cr forms the major oxide in the passive films and
343 CrO_x accounts for ~52 at. %, indicating Cr played a critical role in the anti-corrosion
344 performance. The composition differences of the passive films between CoCrNi
345 monolayer and TaNbHfZr/CoCrNi multilayer coatings are one of the factors that affect

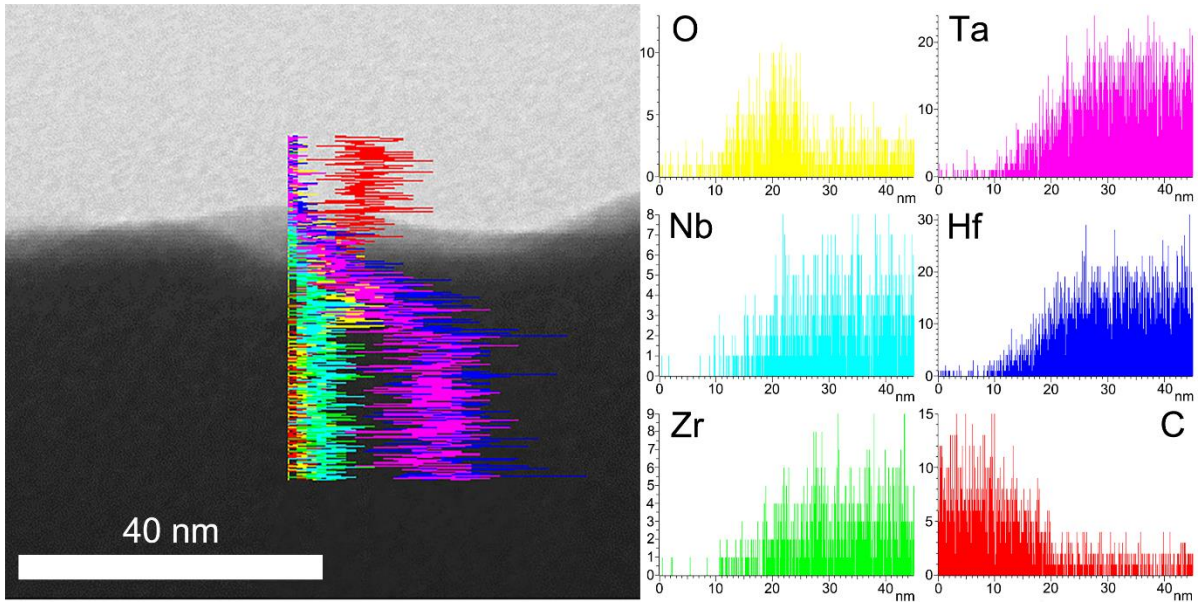
346 their corrosion resistance.



347
348 **Figure 7** XPS spectrum obtained after etching for 120 s by Ar⁺ of Ta 4f, Nb 3d, Hf 4f,
349 Zr 3d and O1s for TaNbHfZr/CoCrNi multilayer coating after immersion of 7 days in
350 the 3.5 wt.% NaCl solution.

351 **3.6.2 TEM-EDS line scan for the passive film**

352 The formation of the passive films relates to the enhancement in corrosion properties
353 of HEAs. The morphology and elemental composition of the passive film were scanned
354 via TEM and EDX, the results are provided in **Figure 8**. The presence of a high
355 concentration of oxygen was confirmed that the oxidation layer with several
356 nanometers in thickness was detected on the surface. The elements of Ta, Nb, Hf and
357 Zr are apt to form the oxidation layer, due to the low Gibbs energy $\Delta_f G^0$ with oxygen
358 (Ta₂O₅: -1911.2 KJ/mol Nb₂O₅: -1766.0 KJ/mol, HfO₂: -1088.2 KJ/mol, ZrO₂: -1042.8
359 KJ/mol) [47]. Additionally, it can be noted that the formation of the oxidation layers is
360 inhomogeneous, confirming that the passive film has weak sites to break down when
361 samples immersed in the Cl⁻ containing environment [48].



362

363 **Figure 8** The TEM image and TEM-EDS line scan result for the top surface of as-
 364 deposited TaNbHfZr/CoCrNi multilayer film.

365 The effective passive film thickness h_{eff} can be calculated using the following relation
 366 [49-51]:

367
$$h_{eff} = \frac{\varepsilon\varepsilon_0 A}{C_{eff}} \quad \text{Equation 3}$$

368 where A is the surface area of the passive film and the effective area is twice of the
 369 geometric area assuming the roughness factor is 2 for the polished specimen [49], ε
 370 is the dielectric constant and the chosen value is 30 for thin films [51, 52], ε_0 is the
 371 vacuum permittivity (8.8542×10^{-14} F/cm), C_{eff} is the effective capacitance of the
 372 passive film extracted from the CPE element to interpret the film properties. The C_{eff}
 373 can be obtained by the following equation [49]:

374
$$C_{eff} = Y_0^{\frac{1}{n}} R_s^{\frac{1-n}{n}} \quad \text{Equation 4}$$

375 where Y_0 is the magnitude of CPE , R_s is the solution resistance, and n is the dispersion
 376 coefficient. The calculated values of C_{eff} and h_{eff} according to **Equations 3** and **4** are
 377 shown in **Table 4**, exhibiting that the thickness of the passive film on the CoCrNi and
 378 TaNbHfZr/CoCrNi coatings are 1.88 nm and 4.42 nm after 30 mins' immersion, and
 379 2.88 nm and 5.75 nm after 7 days' immersion, respectively. The thickness of the
 380 passive film on the multilayer coating of TaNbHfZr/CoCrNi is thicker than that of
 381 CoCrNi monolayer coating, which contributes to the improved corrosion performance

382 of the multilayer structure.

383 **Table 4** CPE1 parameters, resistance, effective capacitance and thickness of passive
384 films formed on the monolayer and multilayer coatings after different immersion times.

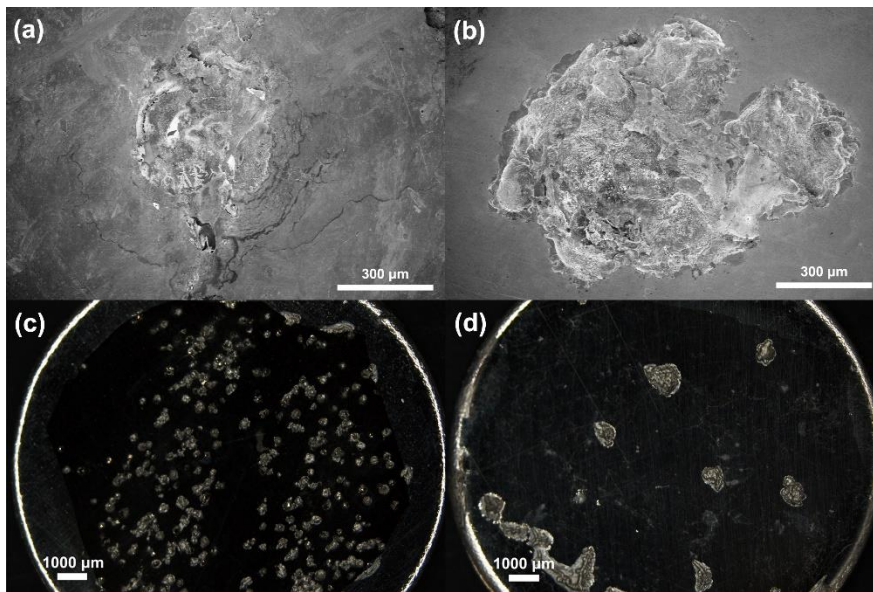
Immersion time	Coating	C_{eff} ($\mu\text{F}/\text{cm}^2$)	h_{eff} (nm)
30 mins	CoCrNi	31.83 ± 1.19	1.88 ± 0.07
	TaNbHfZr/CoCrNi	15.26 ± 0.19	4.42 ± 0.06
7 days	CoCrNi	18.48 ± 0.05	2.88 ± 0.02
	TaNbHfZr/CoCrNi	9.24 ± 0.16	5.75 ± 0.10

385 The excellent corrosion protection of the multilayer coatings comes from the novel
386 multilayer structure. It is well-known that grain boundaries provide more paths for
387 vacancies transport with an irregular atom array. Compared with the crystalline
388 monolayer, the notable enhancement of the corrosion resistance of multilayer coatings
389 with lower i_{corr} and more noble E_{corr} can be ascribed by the existence of the multilayer
390 structure, in which the introduction of the amorphous TaNbHfZr layer without any ready
391 path cut off the diffusion tunnel for localized attack by Cl^- . The interfaces not only cut
392 off the continuous grain boundaries along the texture direction as the hindrance for
393 transporting Cl^- , but also prohibit and block the active sites, resulting in good general
394 corrosion resistance.

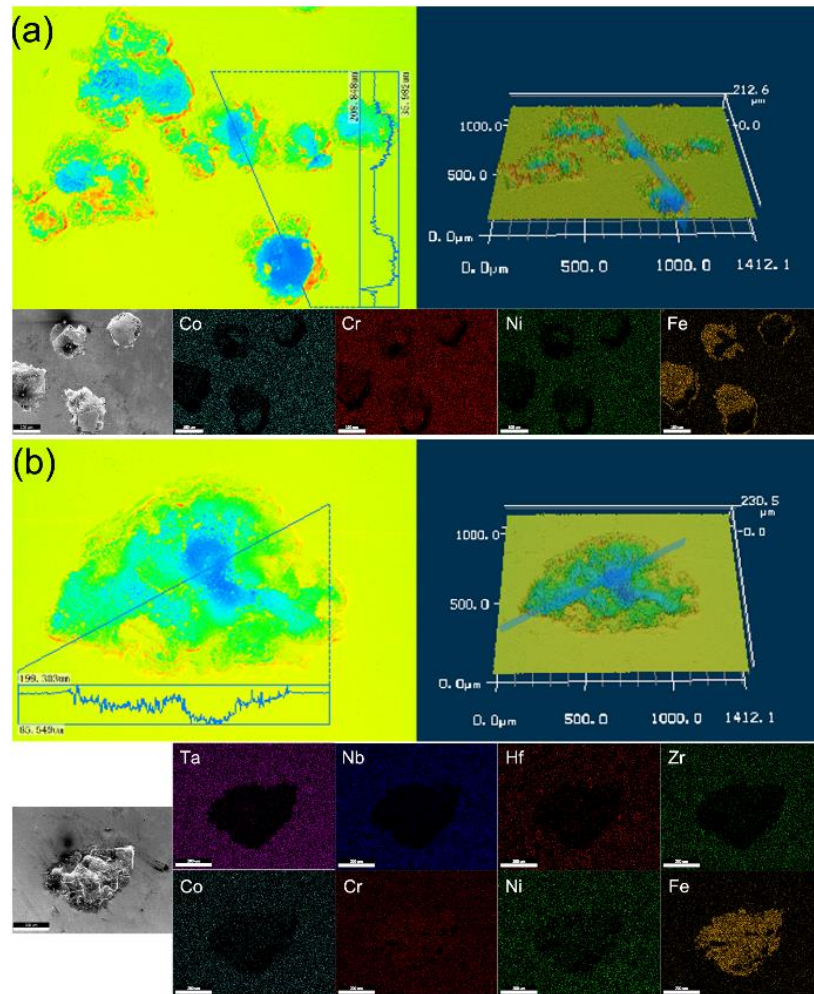
395 **3.7 Characterization of pitting behavior**

396 **Figure 9** exhibits the surface morphologies of CoCrNi monolayer and
397 TaNbHfZr/CoCrNi multilayer coatings after the polarization measurements. To further
398 obtain the depth and compositional distribution of the pits on the surface, 3D
399 profilometry measurement and EDS mapping were carried out, and the results are
400 demonstrated in **Figure 10**. The maximum pitting depth is denoted as h_{max} , and the
401 values of h_{max} for CoCrNi and TaNbHfZr/CoCrNi were $117 \mu\text{m}$ and $131 \mu\text{m}$, respectively.
402 The average pit depth of \bar{h} for CoCrNi coating was $105.2 \pm 6.37 \mu\text{m}$, and $119.3 \pm$
403 $10.22 \mu\text{m}$ for TaNbHfZr/CoCrNi coating. The EDS mapping results show that the
404 apparent contrast difference for intrinsic compositional elements of the coatings and
405 304 SS (e.g. Fe), where the substrate was observed, confirming that the coatings were
406 destroyed after the polarization.

407 As exhibited in **Figures 9 and 10**, fewer and deeper pits appeared on the surface of
408 TaNbHfZr/CoCrNi multilayer coating, while the shallower pits were observed on the
409 CoCrNi monolayer coating surface. The results suggest that the multilayer structure
410 prevents the initiation and propagation of pitting by blocking the corrosive species. *i.e.*
411 grain boundaries or micro-pores which can be disconnected and provided less
412 diffusion channels to transport the corrosive medium, thus pits with less density were
413 observed on the TaNbHfZr/CoCrNi multilayer coating.



414
415 **Figure 9** SEM images for the typical pitting morphologies on the surface of **(a)** CoCrNi
416 and **(b)** TaNbHfZr/CoCrNi multilayer coatings after potentiodynamic polarization test;
417 whole surface morphologies of pitting of **(c)** CoCrNi monolayer and **(d)**
418 TaNbHfZr/CoCrNi multilayer coatings after potentiodynamic polarization.

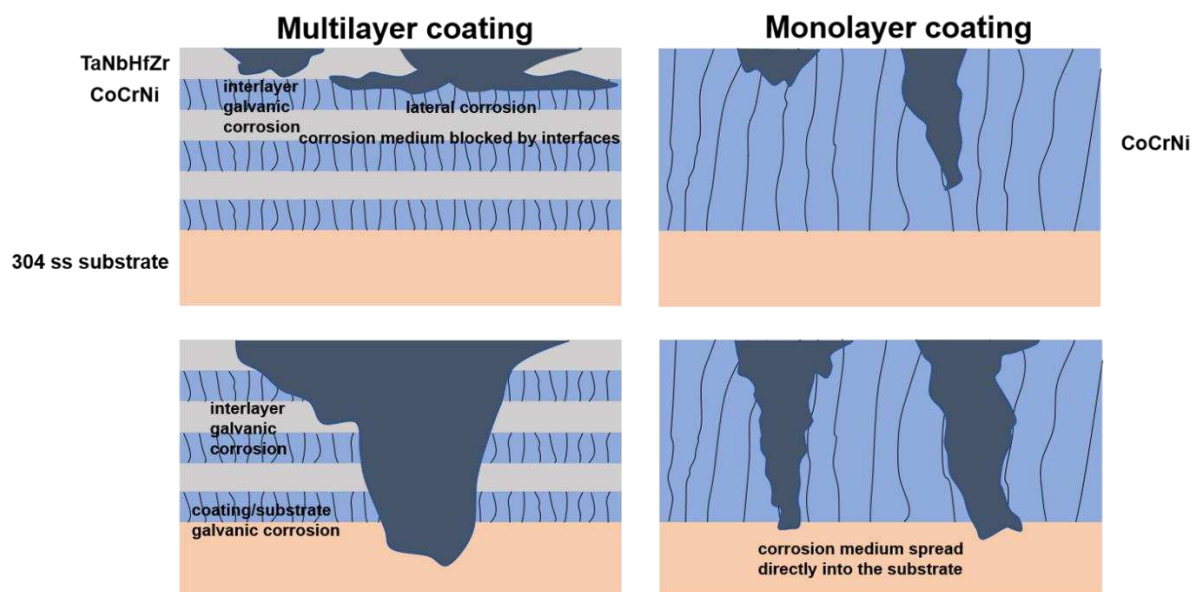


419

420 **Figure 10** Typical 3D morphology and elemental distributions for pitting of **(a)** CoCrNi
 421 and **(b)** TaNbHfZr/CoCrNi multilayer coatings.

422 Galvanic corrosion plays a vital matter to understand the development of localized
 423 corrosion, according to the conception of galvanic corrosion that occurs when the
 424 electrically coupled dissimilar metals exposed in a corrosive environment [53, 54],
 425 CoCrNi monolayer coating has been less affected by the galvanic corrosion based on
 426 the same constituent Cr element with the substrate. The continuous columnar grains
 427 provide plenty of grain boundaries, which are considered as the diffusion channels and
 428 potentially prone sites for pitting [55, 56], increasing the localized corrosion. By
 429 contrast, the introduction of TaNbHfZr into the multilayer deteriorates the resistance to
 430 the localized corrosion via the mutual function of galvanic corrosion between each
 431 interlayer. TaNbHfZr coating with less noble E_{corr} (-0.40 V) acts as the anode upon
 432 coupling compared to that of CoCrNi sublayer (-0.24 V) and steel substrate (-0.33 V)

433 and will be preferentially dissolved. As shown in the schematic diagram in **Figure 11**,
 434 the multilayer interfaces act as the diffusion barriers and block the corrosion medium
 435 to the surface, and the interconnected pores or cracks can be reduced via the
 436 existence of interfaces in the multilayer [57]. Furthermore, the interfaces allow
 437 spreading of the corrosive medium laterally, delaying the attack to the substrate and
 438 lagging the corrosion rate in the multilayer coating [58]. However, once the corrosive
 439 medium reaches the substrate, galvanic corrosion will be triggered among TaNbHfZr
 440 layer, CoCrNi layer and the substrate, in which case the TaNbHfZr layer corrodes
 441 preferentially and accelerates both the penetration of corrosive medium and pit
 442 propagation of the surface. Another point worth mentioning during the pitting process
 443 is the stress caused by the increased volume due to the corrosion products [59]. The
 444 existed products within the corroded layers provide high stresses between the
 445 interfaces or each layer [59], accelerating the enlargement of the pitting size or
 446 microcracks.



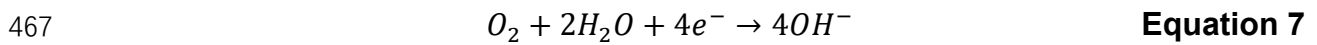
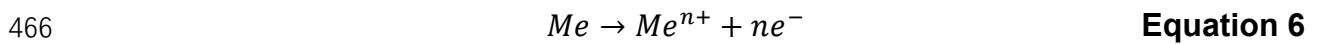
447
 448 **Figure 11** Schematic diagram of corrosion mechanisms in TaNbHfZr/CoCrNi
 449 multilayer and CoCrNi monolayer coatings.

450 Furthermore, the presence of a high concentration of Cr within CoCrNi coating
 451 provides the dissolution of Cr^{3+} ions, which can effectively accelerate the formation of
 452 the passive film as confirmed in **Figure S2** with preferable resistance against the

453 pitting corrosion based on the self-repairing, stable and adherent capability of the
454 passive film [60, 61]. For the multilayer coating of TaNbHfZr/CoCrNi, the top layer of
455 TaNbHfZr has a slow growth rate and inferior recovery ability of the passive film
456 compared to that of CoCrNi coating. Therefore, further work should be considered on
457 the modification of the composition or sequences of each layer to enhance the pitting
458 resistance of the multilayer coating.

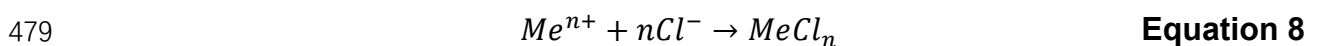
459 **3.7.1 Cl⁻ penetration**

460 The passive films are generated by the oxidation of the compositional elements on the
461 surface and act as a protection layer against corrosion. After the breakdown of the
462 passivity, the pitting corrosion can be attributed to the fact that the anodic sites with
463 fast metal dissolution, but the corresponding cathodic sites can be spread out over a
464 wide range [62]. The related processes can be expressed using the equations as
465 follows:



468 where “Me” represents compositional metals in the coatings, **Equation 6** denotes the
469 anode reaction in which the metals dissolve and the **Equation 7** signifies the cathode
470 reaction with the electron conduction. The passive films are in dynamic equilibrium
471 between film growth and dissolution, among which the dissolution of the film is the
472 electrochemical reaction accompanied by the generation of metal cations [63]. The
473 positively charged metallic ions Ta⁵⁺, Nb⁵⁺, Hf⁴⁺ and Zr⁴⁺ flow into the solution,
474 simultaneously the negatively charged free electron e⁻ pass through the pore solution
475 to the cathode (passive areas), where they are absorbed by oxygen and water to form
476 hydroxyl ions (cathodic reaction).

477 Chlorides enter the pore either by diffusion (in stationary pore water) or by capillary
478 suction of the surface water [64, 65]. The corresponding reactions of Cl⁻ are:



481 It is well known that the Cl⁻ ions possess high permeability with a small ionic radius

482 and can be easily absorbed on the surface of metals as confirmed by **Equation 8**.
483 Local acidification occurs through the hydrolysis of the metal cations, and Cl^- migrate
484 into the pit to balance the charge of the dissolved metal cations and maintain
485 electroneutrality as evidenced by **Equation 9** [66]. The absorption and accumulation
486 of Cl^- increase the donor density of the formed passive film causing a larger potential
487 drop at the film/solution interface, which accelerates the dissolution of the passive film
488 and enlarges or deepens the pitting sites [44]. Additionally, the penetration of Cl^-
489 remarkably modifies the interface via lattice expansion and induces undulation at the
490 material interface [48]. For the multilayer coating of TaNbHfZr/CoCrNi, the introduction
491 of an amorphous TaNbHfZr layer acts as a barrier to reduce the diffusion of Cl^- ions.
492 On the other hand, the multilayer structure decreases the corrosion behaviour by
493 increasing the hindrance between the corrosion environment and the substrate.
494 However, once the pitting occurs, the less anti-corrosive against pitting is the major
495 deficiency for the multilayer coating. Therefore, further work needs to be done to
496 enhance the pitting resistance regarding the optimization of the structure or the
497 chemical composition of the multilayer coating.

498 **4. Conclusion**

499 In this work, we firstly designed and prepared the TaNbHfZr/CoCrNi multilayer coating
500 with amorphous/fcc bi-phase structure combining the concept of high entropy metallic
501 glass with the medium entropy alloy in an anti-corrosive coating system by magnetron
502 sputtering. The passivation behaviour and mechanical properties of the coating have
503 been systematically studied via a series of electrochemical methods and advanced
504 surface analysis. The nanoindentation results indicate that the hardness reduced due
505 to the softening of the shear band induced by the amorphous TaNbHfZr layer and the
506 decreased E_r is the result of the brought inelastic strain by the interfaces. The interface
507 blocking and Hall-Petch strengthening play a joint role in the multilayer strengthening.
508 In a 3.5 wt.% NaCl environment, the corrosion performance of the TaNbHfZr/CoCrNi
509 multilayer coating indicates a more noble corrosion potential and lower current density
510 compared with CoCrNi monolayer coating. The novel multilayer structure plays a key

511 role in corrosion enhancement where the multi-principal components ensure excellent
512 mechanical property and an effective protection mechanism of the Cl⁻ ions induced
513 localized corrosion even in a long-term immersion. However, further work should be
514 focused on the modification of the microstructure, to enhance the pitting resistance of
515 the multilayer coating.

516 **Declaration of competing interest**

517 On behalf of all the authors, we declare that we have no declarations of interest.

518 **Acknowledgments**

519 This work was supported by the Natural Science Foundation of Shaanxi Province (No.
520 2019TD-020).

521 **References**

- 522 [1] J.W. Yeh, S.K. Chen, S.J. Lin, J.Y. Gan, T.S. Chin, T.T. Shun, C.H. Tsau, S.Y. Chang, Nanostructured high-
523 entropy alloys with multiple principal elements: novel alloy design concepts and outcomes, *Adv. Eng.*
524 *Mater.*, 6 (2004) 299-303.
- 525 [2] H. Luo, Z. Li, A.M. Mingers, D. Raabe, Corrosion behavior of an equiatomic CoCrFeMnNi high-entropy
526 alloy compared with 304 stainless steel in sulfuric acid solution, *Corros. Sci.*, 134 (2018) 131-139.
- 527 [3] P. Muangtong, A. Rodchanarowan, D. Chaysuwan, N. Chanlek, R. Goodall, The corrosion behaviour of
528 CoCrFeNi-x (x = Cu, Al, Sn) high entropy alloy systems in chloride solution, *Corros. Sci.*, 172 (2020).
- 529 [4] O.N. Senkov, G.B. Wilks, D.B. Miracle, C.P. Chuang, P.K. Liaw, Refractory high-entropy alloys,
530 *Intermetallics*, 18 (2010) 1758-1765.
- 531 [5] A. Karati, K. Gurusamy, V.S. Hariharan, B.S. Murty, Thermal stability of AlCoFeMnNi high-entropy
532 alloy, *Scr. Mater.*, 162 (2019) 465-467.
- 533 [6] D.B. Miracle, O.N. Senkov, A critical review of high entropy alloys and related concepts, *Acta Mater.*,
534 122 (2017) 448-511.
- 535 [7] M.H. Tsai, J.W. Yeh, High-entropy alloys: A critical review, *Mater. Res. Lett.*, 2 (2014) 107-123.
- 536 [8] Y. Qiu, S. Thomas, M.A. Gibson, H.L. Fraser, N. Birbilis, Corrosion of high entropy alloys, *npj Mater.*
537 *Degrad.*, 1 (2017) 15.
- 538 [9] B.R. Song, Y.H. Li, K.H. Wang, Z.H. Cong, B. Gao, Z.X. Song, J. Chen, Nano-mechanical properties of
539 TaNbHfZr metallic glass films, *Surf. Eng.*, 35 (2019) 728-735.
- 540 [10] Y. Shi, B. Yang, P.K. Liaw, Corrosion-resistant high-entropy alloys: a review, *Metals-Basel*, 7 (2017).
- 541 [11] J. Wang, W. Li, H. Yang, H. Huang, S. Ji, J. Ruan, Z. Liu, Corrosion behavior of CoCrNi medium-entropy
542 alloy compared with 304 stainless steel in H₂SO₄ and NaOH solutions, *Corros. Sci.*, 177 (2020).
- 543 [12] K. Feng, Y. Zhang, Z. Li, C. Yao, L. Yao, C. Fan, Corrosion properties of laser cladded CrCoNi medium
544 entropy alloy coating, *Surf. Coat. Tech.*, 397 (2020).
- 545 [13] S. Zhang, C.L. Wu, C.H. Zhang, M. Guan, J.Z. Tan, Laser surface alloying of FeCoCrAlNi high-entropy
546 alloy on 304 stainless steel to enhance corrosion and cavitation erosion resistance, *Opt. Laser Technol.*, 84
547 (2016) 23-31.
- 548 [14] F. Cao, P. Munroe, Z. Zhou, Z. Xie, Medium entropy alloy CoCrNi coatings: Enhancing hardness and
549 damage-tolerance through a nanotwinned structuring, *Surf. Coat. Tech.*, 335 (2018) 257-264.

550 [15] Z. Wu, H. Bei, F. Otto, G.M. Pharr, E.P. George, Recovery, recrystallization, grain growth and phase
551 stability of a family of FCC-structured multi-component equiatomic solid solution alloys, *Intermetallics*, 46
552 (2014) 131-140.

553 [16] M.A. Ezazi, M.M. Quazi, E. Zalnezhad, A.A.D. Sarhan, Enhancing the tribo-mechanical properties of
554 aerospace AL7075-T6 by magnetron-sputtered Ti/TiN, Cr/CrN & TiCr/TiCrN thin film ceramic coatings,
555 *Ceram. Int.*, 40 (2014) 15603-15615.

556 [17] R.D. Arnell, P.J. Kelly, Recent advances in magnetron sputtering, *Surf. Coat. Tech.*, 112 (1999) 170-176.

557 [18] A.A. Voevodin, J.P. O'Neill, J.S. Zabinski, Nanocomposite tribological coatings for aerospace
558 applications, *Surf. Coat. Tech.*, 116-119 (1999) 36-45.

559 [19] P.E. Hovsepian, Q. Luo, G. Robinson, M. Pittman, M. Howarth, D. Doerwald, R. Tietema, W.M. Sim, A.
560 Deeming, T. Zeus, TiAlN/VN superlattice structured PVD coatings: a new alternative in machining of
561 aluminium alloys for aerospace and automotive components, *Surf. Coat. Tech.*, 201 (2006) 265-272.

562 [20] V.V.A. Thampi, A. Bendavid, B. Subramanian, Nanostructured TiCrN thin films by pulsed magnetron
563 sputtering for cutting tool applications, *Ceram. Int.*, 42 (2016) 9940-9948.

564 [21] S. Hong, S.H. Kang, Y. Kim, C.W. Jung, Transparent and flexible antenna for wearable glasses
565 applications, *IEEE T. Antenn Propag.*, 64 (2016) 2797-2804.

566 [22] W. Li, P. Liu, P.K. Liaw, Microstructures and properties of high-entropy alloy films and coatings: a review,
567 *Mater. Res. Lett.*, 6 (2018) 199-229.

568 [23] Z. An, H. Jia, Y. Wu, P.D. Rack, A.D. Patchen, Y. Liu, Y. Ren, N. Li, P.K. Liaw, Solid-solution CrCoCuFeNi
569 high-entropy alloy thin films synthesized by sputter deposition, *Mater. Res. Lett.*, 3 (2015) 203-209.

570 [24] L. Liu, J.B. Zhu, C. Hou, J.C. Li, Q. Jiang, Dense and smooth amorphous films of multicomponent
571 FeCoNiCuVZrAl high-entropy alloy deposited by direct current magnetron sputtering, *Mater. Design*, 46
572 (2013) 675-679.

573 [25] Y. Yan, J. Lee, X.L. Cui, Enhanced photoelectrochemical properties of Ta-TiO₂ nanotube arrays
574 prepared by magnetron sputtering, *Vacuum*, 138 (2017) 30-38.

575 [26] J.H. Huang, C.H. Ma, H. Chen, Effect of Ti interlayer on the residual stress and texture development of
576 TiN thin films deposited by unbalanced magnetron sputtering, *Surf. Coat. Technol.*, 201 (2006) 3199-3204.

577 [27] J. Creus, H. Idrissi, H. Mazille, F. Sanchette, P. Jacquot, Improvement of the corrosion resistance of CrN
578 coated steel by an interlayer, *Surf. Coat. Tech.*, 107 (1998) 183-190.

579 [28] S. Guo, C.T. Liu, Phase stability in high entropy alloys: formation of solid-solution phase or amorphous
580 phase, *Prog. Nat. Sci-Mater.*, 21 (2011) 433-446.

581 [29] Z. Li, C.H. Liu, Q.S. Chen, J.J. Yang, J.M. Liu, H.Y. Yang, W. Zhang, R.Q. Zhang, L.X. He, J.P. Long, H.
582 Chang, Microstructure, high-temperature corrosion and steam oxidation properties of Cr/CrN multilayer
583 coatings prepared by magnetron sputtering, *Corros. Sci.*, 191 (2021).

584 [30] R.Z. Li, S.H. Wang, J.B. Pu, D.P. Zhou, M. Yu, Y. Wei, W.M. Guo, Study of NaCl-induced hot-corrosion
585 behavior of TiN single-layer and TiN/Ti multilayer coatings at 500 °C, *Corros. Sci.*, 192 (2021).

586 [31] W.C. Oliver, G.M. Pharr, An improved technique for determining hardness and elastic-modulus using
587 load and displacement sensing indentation experiments, *J. Mater. Res.*, 7 (1992) 1564-1583.

588 [32] N.G. Chechenin, J. Bottiger, J.P. Krog, Nanoindentation of amorphous aluminum oxide films I. The
589 influence of the substrate on the plastic properties, *Thin Solid Films*, 261 (1995) 219-227.

590 [33] M. Callisti, T. Polcar, Combined size and texture-dependent deformation and strengthening
591 mechanisms in Zr/Nb nano-multilayers, *Acta Mater.*, 124 (2017) 247-260.

592 [34] W.D. Nix, Yielding and strain hardening of thin metal films on substrates, *Scr. Mater.*, 39 545.

593 [35] W.H. Liu, Y. Wu, J.Y. He, T.G. Nieh, Z.P. Lu, Grain growth and the Hall-Petch relationship in a high-

594 entropy FeCrNiCoMn alloy, *Scripta Mater.*, 68 (2013) 526-529.

595 [36] Z.H. Cao, Y.J. Ma, Y.P. Cai, G.J. Wang, X.K. Meng, High strength dual-phase high entropy alloys with a
596 tunable nanolayer thickness, *Scr. Mater.*, 173 (2019) 149-153.

597 [37] Z. Fu, W. Chen, H. Wen, D. Zhang, Z. Chen, B. Zheng, Y. Zhou, E.J. Lavernia, Microstructure and
598 strengthening mechanisms in an FCC structured single-phase nanocrystalline Co₂₅Ni₂₅Fe₂₅Al_{7.5}Cu_{17.5}
599 high-entropy alloy, *Acta Mater.*, 107 (2016) 59-71.

600 [38] P. Goudeau, P. Villain, T. Girardeau, P.O. Renault, K.F. Badawi, Elastic constants investigation by X-ray
601 diffraction of in situ deformed metallic multi-layers, *Scr. Mater.*, 50 (2004) 723-727.

602 [39] M.H. Allahyarzadeh, M. Aliofkhaezai, A.S. Rouhaghdam, V. Torabinejad, H. Alimadadi, A. Ashrafi,
603 Electrodeposition mechanism and corrosion behavior of multilayer nanocrystalline nickel-tungsten alloy,
604 *Electrochim. Acta*, 258 (2017) 883-899.

605 [40] S. Eriksson, H.P. Hermansson, Pitting corrosion of copper in nuclear waste disposal environments, in,
606 Sweden, 1997, pp. 94.

607 [41] Y. Li, J. Xu, Is niobium more corrosion-resistant than commercially pure titanium in fluoride-containing
608 artificial saliva?, *Electrochim. Acta*, 233 (2017) 151-166.

609 [42] W. Wang, F. Mohammadi, A. Alfantazi, Corrosion behaviour of niobium in phosphate buffered saline
610 solutions with different concentrations of bovine serum albumin, *Corros. Sci.*, 57 (2012) 11-21.

611 [43] X. Yue, L. Zhang, Y. Hua, J. Wang, N. Dong, X. Li, S. Xu, A. Neville, Revealing the superior corrosion
612 protection of the passive film on selective laser melted 316L SS in a phosphate-buffered saline solution,
613 *Appl. Surf. Sci.*, 529 (2020).

614 [44] Z. Duan, C. Man, C. Dong, Z. Cui, D. Kong, L. Wang, X. Wang, Pitting behavior of SLM 316L stainless
615 steel exposed to chloride environments with different aggressiveness: Pitting mechanism induced by gas
616 pores, *Corros. Sci.*, 167 (2020).

617 [45] S. Fajardo, D.M. Bastidas, M. Criado, J.M. Bastidas, Electrochemical study on the corrosion behaviour
618 of a new low-nickel stainless steel in carbonated alkaline solution in the presence of chlorides, *Electrochim.*
619 *Acta*, 129 (2014) 160-170.

620 [46] G. Okamoto, Passive film of 18-8 stainless steel structure and its function, *Corros. Sci.*, 13 (1973) 471-
621 489.

622 [47] D.R. Lide, K.S. Lide, *CRC handbook of chemistry and physics*, (2001-2002).

623 [48] B. Zhang, J. Wang, B. Wu, X.W. Guo, Y.J. Wang, D. Chen, Y.C. Zhang, K. Du, E.E. Oguzie, X.L. Ma,
624 Unmasking chloride attack on the passive film of metals, *Nat. Commun.*, 9 (2018) 2559.

625 [49] Z. Cui, S. Chen, Y. Dou, S. Han, L. Wang, C. Man, X. Wang, S. Chen, Y. Cheng, X. Li, Passivation behavior
626 and surface chemistry of 2507 super duplex stainless steel in artificial seawater: Influence of dissolved
627 oxygen and pH, *Corros. Sci.*, 150 (2019) 218-234.

628 [50] B. Hirschorn, M.E. Orazem, B. Tribollet, V. Vivier, I. Frateur, M. Musiani, Determination of effective
629 capacitance and film thickness from constant-phase-element parameters, *Electrochim. Acta*, 55 (2010)
630 6218-6227.

631 [51] A. Kocijan, D.K. Merl, M. Jenko, The corrosion behaviour of austenitic and duplex stainless steels in
632 artificial saliva with the addition of fluoride, *Corros. Sci.*, 53 (2011) 776-783.

633 [52] D. Wallinder, J. Pan, C. Leygraf, A. Delblanc-Bauer, EIS and XPS study of surface modification of
634 316LVM stainless steel after passivation, *Corros. Sci.*, 41 (1999) 275-289.

635 [53] F. Mansfeld, D.H. Hengstenberg, J.V. Kenkel, Galvanic corrosion of Al alloys I. effect of dissimilar metal,
636 *Corrosion-Us*, 30 (1974) 343-353.

637 [54] Calculation of sputter etch rates.

638 [55] Z. Yan, L. Guo, Z. Li, Y. Yu, Q. He, Effects of laser glazing on CMAS corrosion behavior of Y₂O₃ stabilized
639 ZrO₂ thermal barrier coatings, *Corros. Sci.*, 157 (2019) 450-461.

640 [56] M.H. Allahyarzadeh, M. Aliofkhaezraei, A.R.S. Rouhaghdam, V. Torabinejad, Electrochemical tailoring of
641 ternary Ni-W-Co(Al₂O₃) nanocomposite using pulse reverse technique, *J. Alloys Compd.*, 705 (2017) 788-
642 800.

643 [57] V. Torabinejad, M. Aliofkhaezraei, A. Sabour Rouhaghdam, M.H. Allahyarzadeh, Ni-Fe-Mn-(nano)Al₂O₃
644 Coating with Modulated Composition and Grain Size, *T. Indian I. Metals*, 70 (2016) 1199-1207.

645 [58] V. Bonu, M. Jeevitha, V.P. Kumar, G. Srinivas, Siju, H.C. Barshilia, Solid particle erosion and corrosion
646 resistance performance of nanolayered multilayered Ti/TiN and TiAl/TiAlN coatings deposited on Ti6Al4V
647 substrates, *Surf. Coat. Tech.*, 387 (2020).

648 [59] V. Torabinejad, M. Aliofkhaezraei, A. Sabour Rouhaghdam, M.H. Allahyarzadeh, Corrosion properties of
649 Ni-Fe-Cr (III) multilayer coating synthesized via pulse duty cycle variation, *Mater. Corros.*, 68 (2017) 347-
650 354.

651 [60] M. Urretabizkaya, C.D. Pallotta, N.D. Cristofaro, R.C. Salvarezza, A.J. Arvia, Changes in the composition
652 of the passive layer and pitting corrosion of stainless steel in phosphate-borate buffer containing chloride
653 ions, *Electrochim. Acta*, 33 (1988) 1645-1651.

654 [61] R.T. Loto, Pitting corrosion evaluation of austenitic stainless steel type 304 in acid chloride media, *J.*
655 *Mater. Environ. Sci.*, 4 (2013) 448-459.

656 [62] C.A. Apostolopoulos, S. Demis, V.G. Papadakis, Chloride-induced corrosion of steel reinforcement –
657 mechanical performance and pit depth analysis, *Constr. Build. Mater.*, 38 (2013) 139-146.

658 [63] D.D. Macdonald, The history of the point defect model for the passive state: a brief review of film
659 growth aspects, *Electrochim. Acta*, 56 (2011) 1761-1772.

660 [64] C.L. Page, K.W.J. Treadaway, Aspects of the electrochemistry of steel in concrete, *Nature*, 297 (1982)
661 109-115.

662 [65] J. Ožbolt, G. Balabanić, G. Periškić, M. Kušter, Modelling the effect of damage on transport processes
663 in concrete, *Constr. Build. Mater.*, 24 (2010) 1638-1648.

664 [66] T. Li, J.R. Scully, G.S. Frankel, Localized corrosion: passive film breakdown vs. pit growth stability: part
665 III. a unifying set of principal parameters and criteria for pit stabilization and salt film formation, *J.*
666 *Electrochem. Soc.*, 165 (2018) C762-C770.

667